Ring-Diagram Analysis with GONG++ (first Draft)

T. Corbard

July 1, 2003

Abstract

Images from the updated GONG network (GONG+) have been produced since July 2001. In order to treat individual site images and the merged images (Toner et al., 2003) for local helioseismology studies, we have developed an enhanced tracking/remapping code that is now part of the new GONG pipeline (GONG++) (Hill et al., 2003). We present here the tools for producing the data-cube, 3D power spectra and sub-surface flow maps that will become part of the new GONG++ products and compare the preliminary results with the ring diagram analysis of MDI images for the same days.

1 Scientific Objectives

Ring-diagram analysis of MDI images carried out over the last few years has led to a break-through in helioseismic studies which now allow us to observe the solar sub-surface flows in both azimuthal and meridional directions and in both solar hemispheres. Using this analysis technique one can study plasma dynamics around and below surface magnetic features and their evolution during the solar cycle or at smaller time scales. It remains unclear however what the uncertainties and potential bias on these measurements might be. The new high resolution GONG+ observations will allow us to test these important results with independent datasets and to insure the continuity for the production of the so-called sub-surface solar weather flow maps during and after the spatial missions SOHO and SDO.

2 Producing the 'data cube': splitup.f90

2.1 Steps and Definitions

In order to estimate the mean 3D velocities of an area over the Sun we need to follow this area over time. Such a spatio-temporal area is defined by an array (or *data-cube*) of $N_x \times N_y \times N_t$ points $M_{ij}(t_k)$ identified by their heliographic latitudes $\psi_{ij}(t_k)$ and Carrington longitude $\varphi_{ij}(t_k)$ at different times t_k. In order to define such an area completely we need:

1. **A reference time** t_0 **and a central position** $M_0 = M_{00}(t_0)$ given by $\psi_0 = \psi_{00}(t_0)$ and $\varphi_0 = \varphi_{00}(t_0)$.
2. **A sampling time** Δt so that $t_k = t_0 + k\Delta t$ for $k = -N_t/2 + 1..N_t/2$

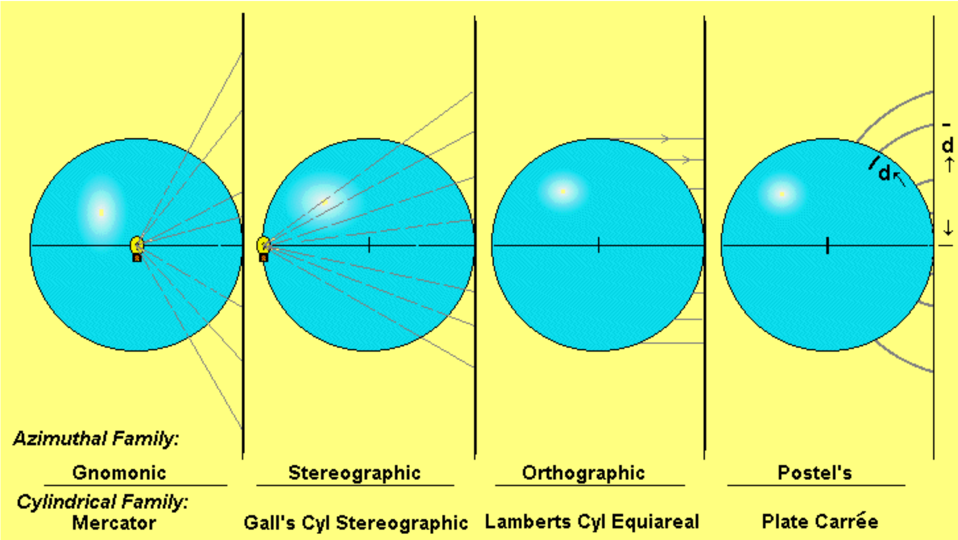

Figure 1: A Classification of Projections. From http://www.hig.se/ dds/teach/projwrk1/consec2.htm

3. The definition of a collection of points around the central position (remapping) and a tracking rate for following these points in time.

$$\left\{ \begin{array}{l} \psi_0 \\ \varphi_0 \end{array} \right. \xrightarrow{\textbf{remapping}} \left\{ \begin{array}{l} \psi_{ij}(t_0) \\ \varphi_{ij}(t_0) \end{array} \right. \xrightarrow{\textbf{tracking}} \left\{ \begin{array}{l} \psi_{ij}(t_k) \\ \varphi_{ij}(t_k) \end{array} \right.$$

4. The definition of the **camera projection** that gives the fractional camera pixels for a given heliographic latitude and longitude.

5. **An interpolator** in order to estimate the values of the Doppler velocities at the wanted fractional pixels from the recorded image pixel values.

2.2 Remapping

For our local analysis, the high degree acoustic waves are assumed to be plane waves traveling across the surface of the Sun following geodesics i.e. great circles. Moreover we are going to use a 3D Fourier transform for which equidistance is assumed. Therefore we would like to have a grid on which each horizontal or vertical line is a great circle and where the distances are preserved in both directions (the equidistance in time being provided by the constant image rate Δt). In a gnomic projection (see Fig. 1), the point of projection is the centre of the sphere and therefore each straight line would represent a great circle but the distance scale is greatly distorted. Unfortunately, no projection can be made that preserves distance along the entire extent of the line joining any two points. However the equidistance can be insured, at least in one direction, without too much distortion near the center of the projection.

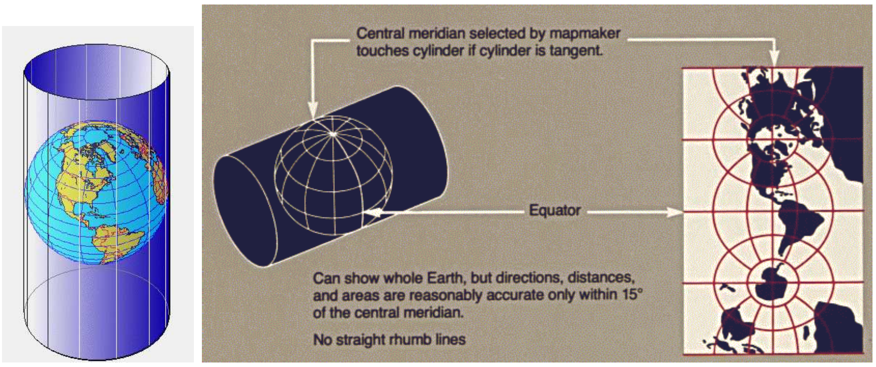

Figure 2: Cylindrical projections. In the normal aspect (left) the tangent line is the equator and all meridians are mapped as vertical straight lines. In the transverse aspect (right), the tangent line is a meridian and each horizonthal line of the map is describing a great circle orthogonal to the meridian of tangency. From http://www.hig.se/ dds/teach/projwrk1/merctran.htm

2.2.1 The transverse cylindrical equidistant projection

The projection used is a *transverse cylindrical equidistant projection* (or transverse plate carrée, see Figs. 1, 2). *Cylindrical* means that it is constructed by wrapping a cylinder around the sphere. All great circles orthogonal to the one tangent to the cylinder will be remapped as parallel straight lines. It is called *transverse* because the tangent great circle chosen is not the equator but rather the solar meridian passing through M_0. *Equidistant* means that distance is preserved along the great circles shown as horizontal lines on the remapped area. Finally we note that the points are not geometrically *projected*, in the true sense of the word, i.e. it is not a perspective projection.

If we note R the heliocentric coordinate system, this projection can be obtained by placing a point of heliocentric colatitude and longitude $(\theta, \varphi)_R$ at the map coordinates:

$$\left\{ \begin{array}{ll} X = & -\bar{\psi} = \bar{\theta} - \pi/2 \\ Y = & \bar{\varphi} \end{array} \right. \tag{1}$$

where $\bar{\psi}$ and $\bar{\varphi}$ are respectively the latitude and longitude of that point in a system $\bar{R}$ in which the solar meridian passing through M_0 is the new equator, the x-axis is pointing towards M_0 and the z-axis is towards east. Therefore if we note:

- $M_0(\theta_0, \varphi_0)_R$
- $\mathcal{M}$ the Solar meridian passing through M_0
- $\mathcal{M}_\perp$ the great circle orthogonal to $\mathcal{M}$ and passing through M_0

then, $\bar{R} \equiv (\bar{x} = \sin\bar{\theta}\cos\bar{\varphi},\ \bar{y} = \sin\bar{\theta}\sin\bar{\varphi},\ \bar{z} = \cos\bar{\theta})$ is a coordinate system in which:

$$\left\{\begin{array}{l}\bullet\ O\bar{x} = OM_0 \\ \bullet\ \mathcal{M} \text{ is in the plan } (\bar{x}O\bar{y}) \text{ with } \widehat{\bar{x}O\bar{y}} > 0 \text{ towards north} \\ \quad \mathcal{M}:\ \ \bar{\theta} = \pi/2 \ \ \Leftrightarrow \ \ X = 0 \\ \bullet\ \mathcal{M}_\perp \text{ is in the plan } (\bar{z}O\bar{x}) \text{ with } \widehat{\bar{z}O\bar{x}} > 0 \text{ towards west} \\ \quad \mathcal{M}_\perp:\ \ \bar{\varphi} = 0 \text{ or } \pi \ \ \Leftrightarrow \ \ Y = 0 \text{ or } \pi \end{array}\right.$$

The spherical coordinates $(\bar{\theta}, \bar{\varphi})$ in $\bar{R}$ are obtained from the heliographic coordinates (θ, φ) by the following rotations:

1. $\underline{R \to R' :\ \varphi_0 + \frac{\pi}{2}\ /z}$

$$\left\{\begin{array}{lcl}\varphi' & = & \varphi - \varphi_0 - \frac{\pi}{2} \\ \theta' & = & \theta\end{array}\right.$$

2. $\underline{R' \to R'' :\ \theta_0\ /x'}$

$$\begin{pmatrix} x'' \\ y'' \\ z'' \end{pmatrix} = \begin{pmatrix} 1 & 0 & 0 \\ 0 & \cos\theta_0 & \sin\theta_0 \\ 0 & -\sin\theta_0 & \cos\theta_0 \end{pmatrix} \begin{pmatrix} x' \\ y' \\ z' \end{pmatrix}$$

$$\Rightarrow \left\{\begin{array}{lcl}\sin\theta''\cos\varphi'' & = & \sin\theta\sin(\varphi-\varphi_0) \\ \sin\theta''\sin\varphi'' & = & -\cos\theta_0\sin\theta\cos(\varphi-\varphi_0) + \sin\theta_0\cos\theta \\ \cos\theta'' & = & \sin\theta_0\sin\theta\cos(\varphi-\varphi_0) + \cos\theta_0\cos\theta\end{array}\right. \tag{2}$$

3. $\underline{R'' \to \bar{R} :\ \frac{\pi}{2}\ /y''}$

$$\left\{\begin{array}{l}\bar{x} = z'' \\ \bar{y} = y'' \\ \bar{z} = -x''\end{array}\right. \Rightarrow \left\{\begin{array}{l}\sin\bar{\theta}\cos\bar{\varphi} = \sin\theta_0\sin\theta\cos(\varphi-\varphi_0) + \cos\theta_0\cos\theta \\ \sin\bar{\theta}\sin\bar{\varphi} = -\cos\theta_0\sin\theta\cos(\varphi-\varphi_0) + \sin\theta_0\cos\theta \\ \cos\bar{\theta} = -\sin\theta\sin(\varphi-\varphi_0)\end{array}\right. \tag{3}$$

Equations (1) and (3) define the transverse cylindrical equidistant projection completly. We note that $\bar{\theta}$, and therefore X, are independent of θ_0. This means that, if we change the latitude of the center of projection (keeping the same longitude φ_0), the new map is simply obtained by translating along the Y axis. This is simply because, as said above, in a cylindrical projection there is not a center of projection but rather a line of tangency. In our case the line of tangency is a meridian so if we change θ_0 but keep φ_0, the line of tangency remains the same and therefore the map is the same (Fig. 3).

2.2.2 Reversing the projection

The heliographic latitudes $\psi_{ij}(t_0)$ and longitudes $\varphi_{ij}(t_0)$ for which we want the doppler velocities at $t = t_0$ are then obtained by reversing the projection. We first take points equally spaced in latitude and longitude in $\bar{R}$:

$$\boxed{\left\{\begin{array}{lll}X_i \equiv -\bar{\psi}_i \equiv \bar{\theta}_i - \frac{\pi}{2} & \equiv (i - (N_x+1)/2)\,\Delta x & i = 1..N_x \\ Y_j \equiv \bar{\varphi}_j & \equiv (j - (N_y+1)/2)\,\Delta y & j = 1..N_y\end{array}\right.} \tag{4}$$

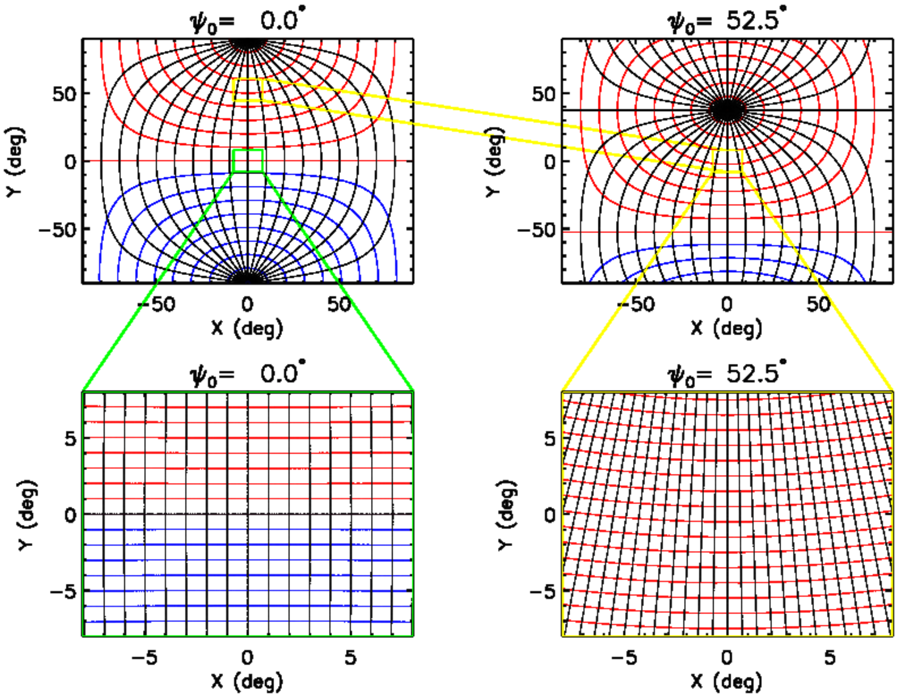

Figure 3: Solar meridians and parallels in the equidistant transverse cylindrical projection with $\psi_0 = 0°$ (upper left) and $\psi_0 = 52.5°$ (upper right). Two close-up around the center are shown in the lower pannels. On the upper figures the spacing is $10°$ while it is $1°$ on the two close-up. As a change of ψ_0 results in just a vertical translation, the upper right figure is just a translation of the upper left one and the lower right figure is also also given by a close-up of the upper left figure around $52.5°$.

where the angular spacings Δx and Δy and the number of points N_x and N_y are chosen so that:

$$\boxed{\begin{cases} |X_i| < \frac{\pi}{2} \quad \forall i & \Leftrightarrow (N_x - 1)\Delta_x < \pi \\ |Y_j + \psi_0| < \frac{\pi}{2} \quad \forall j & \Leftrightarrow (N_y - 1)\Delta_y < \pi - 2|\psi_0| \end{cases}} \tag{5}$$

Then, from (3) and (4), we have:

$$\begin{aligned} \cos X_i \cos Y_j &= \cos\psi_0 \cos\psi_{ij}(t_0)\cos(\varphi_{ij}(t_0) - \varphi_0) + \sin\psi_0 \sin\psi_{ij}(t_0) && (6) \\ \cos X_i \sin Y_j &= -\sin\psi_0 \cos\psi_{ij}(t_0)\cos(\varphi_{ij}(t_0) - \varphi_0) + \cos\psi_0 \sin\psi_{ij}(t_0) && (7) \\ \sin X_i &= \cos\psi_{ij} \sin(\varphi_{ij}(t_0) - \varphi_0) && (8) \end{aligned}$$

$$(6) \Rightarrow \cos\psi_{ij}(t_0)\cos(\varphi_{ij}(t_0) - \varphi_0) = \frac{\cos X_i \cos Y_j - \sin\psi_0 \sin\psi_{ij}(t_0)}{\cos\psi_0} \tag{9}$$

$$\begin{aligned} (7), (9) \Rightarrow \cos X_i \sin Y_j \cos\psi_0 &= -\sin\psi_0 \cos X_i \cos Y_j + \sin\psi_{ij}(t_0) \\ \Leftrightarrow \cos X_i \sin(Y_j + \psi_0) &= \sin\psi_{ij}(t_0) && (10) \end{aligned}$$

$$(10),\ |\psi_{ij}(t_0)| < \frac{\pi}{2} \ \Rightarrow \boxed{\psi_{ij}(t_0) = \arcsin\left(\cos X_i \sin(Y_j + \psi_0)\right)} \tag{11}$$

$$\begin{aligned} (5),\ (9),\ (10) \Rightarrow \cos(\varphi_{ij}(t_0) - \varphi_0) > 0 \quad &\Leftrightarrow \quad \cos Y > \sin\psi_0 \sin(Y + \psi_0) \\ &\Leftrightarrow \quad \cos Y > \sin\psi_0 \sin Y \cos\psi_0 + \cos Y \sin^2\psi_0 \\ &\Leftrightarrow \quad 1 > \tan Y \tan\psi_0 \\ &\Leftrightarrow \quad \frac{\tan Y + \tan\psi_0}{\tan(Y + \psi_0)} > 0 && (12) \end{aligned}$$

- If $\tan(Y + \psi_0) > 0$:

$$(12) \Rightarrow \cos(\varphi_{ij}(t_0) - \varphi_0) > 0 \quad \Leftrightarrow \quad Y + \psi_0 > 0 \Rightarrow 0 < Y + \psi_0 < \frac{\pi}{2}$$

- If $\tan(Y + \psi_0) < 0$:

$$(12) \Rightarrow \cos(\varphi_{ij}(t_0) - \varphi_0) > 0 \quad \Leftrightarrow \quad Y + \psi_0 < 0 \Rightarrow -\frac{\pi}{2} < Y + \psi_0 < 0$$

therefore:

$$(12) \Leftrightarrow |\varphi_{ij}(t_0) - \varphi_0| < \frac{\pi}{2} \Leftrightarrow |Y + \psi_0| < \frac{\pi}{2}, \tag{13}$$

and:

$$(5),\ (8),\ (13) \Rightarrow \boxed{\varphi_{ij}(t_0) = \left\{\arcsin\left(\frac{\sin X_i}{\cos\psi_{ij}(t_0)}\right) + \varphi_0\right\} \quad [2\pi]} \tag{14}$$

where $\{x\}$ $[2\pi]$ means that we may have to add multiples of 2π to x in order to insure $0 \leq x < 2\pi$. This can be done using $x = mod(x + 2\pi, 2\pi)$ where mod is the intrinsic FORTRAN modulo function.

Equations (4), (11) and (14) define the remapping completly once we have chosen $\mathbf{t_0}$, ψ_0, φ_0, $\mathbf{N_x}$, $\mathbf{N_y}$, $\mathbf{\Delta_x}$ and $\mathbf{\Delta_y}$. Note that Eq. (5) must be satisfied for the above equations to be valid but it does not insure that the resulting latitudes and longitudes will be present on the observed disk at $t = t_0$.

We now have defined the heliographic latitudes and longitudes of a collection of points around (ψ_0, φ_0) for which we want to know the doppler velocities at $t = t_0$. The next step is to follow these points in time and define the heliographic latitudes and longitudes for which we want the doppler velocities at all time t_k around t_0. Then we will need to effectively get the values of the doppler velocities at these points from the GONG+ images i.e. we will need to know what are the image coordinates that correspond to a given heliocentric latitude and longitude. We will however first say a bit more about the remapping and discuss the Postel projection which was often refered as the one used in ring-diagram analysis.

2.2.3 Comparison with the Postel projection

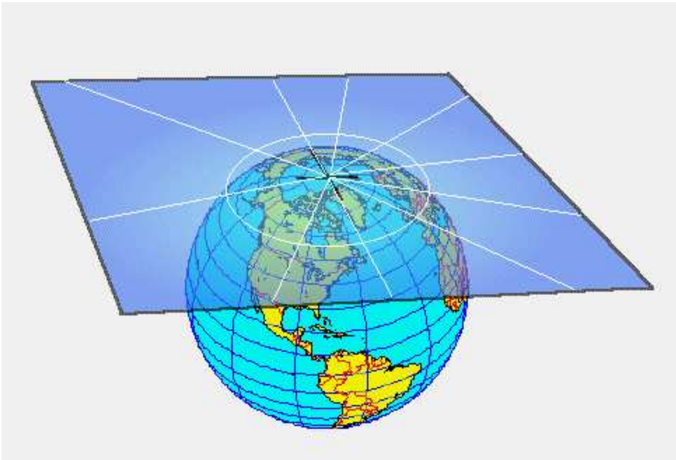

Figure 4: Azimuthal equidistant (Postel) projection in its polar aspect: all straight lines going through the center of projection (here the pole) are great circles.

From http://www.hig.se/ dds/teach/projwrk1/consec2.htm

The azimuthal equidistant (or Postel) projection has also been used for ring analysis (e.g. Bogart et al., 1995). This projection, originally used by Guillaume Postel (1581), is constructed by projecting on a plane tangent to the sphere at M_0 while preserving the distance along the great circles passing through M_0 (Figs. 1, 4). Therefore the distances are preserved on all lines passing through M_0 but not along the line X=constant or Y=constant (except for $X = 0$ and $Y = 0$). It is also not a perspective projection.

On the other hand, when using the transverse cylindrical projection, we see from Eq. (4), that since a line of constant longitude (or meridien) in $\bar{R}$ is a great circle, all horizontal lines (Y=constant) of the remapped area are great circles. Moreover the projection is such that equally spaced points along these lines are also equidistant on the solar surface. The vertical lines (X=contant) are however not describing great circles (they describe parallels in $\bar{R}$) and the distances are not preserved along these lines.

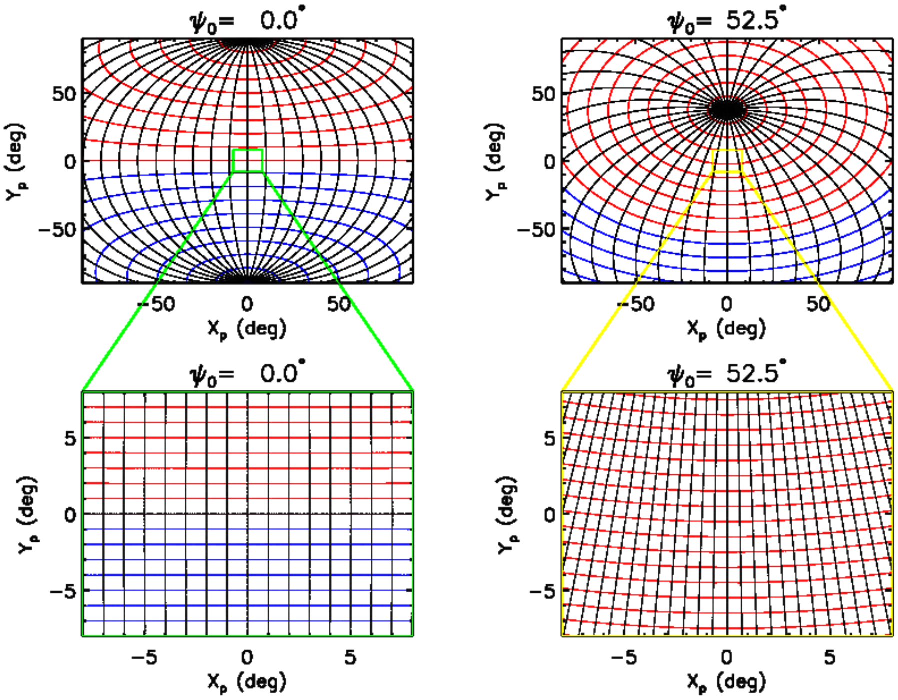

Figure 5: Solar meridians and parallels in the Postel or azimuthal equidistant projection with $\psi_0 = 0°$ (upper left) and $\psi_0 = 52.5°$ (upper right). Two close-up around the center are shown in the lower pannels. On the upper figures the spacing is 10° while it is 1° on the two close-up. Note that the upper right figure is not just a translation of the upper left one. The two lower pannels illustrate, by comparison with Fig. 3, that the equidistant transverse cylindrical and Postel projections are similar for small areas.

The Postel projection is built by placing a point of heliographic coordinate (θ, φ) at the map coordinates:

$$\left\{ \begin{array}{lcl} X_p & = & \theta'' \ \cos\varphi'' \\ Y_p & = & \theta'' \ \sin\varphi'' \end{array} \right. \tag{15}$$

where $(\theta'', \ \varphi'')$ are the spherical coordinates in the system R'' in which:

$$\left\{ \begin{array}{l} \bullet\ M_0 \text{ is at the pole i.e. } 0M_0 = Oz'' \\ \bullet\ \mathcal{M} \text{ is in the plane } (z''0y'') \text{ with } \widehat{z''Oy''} > 0 \text{ towards north} \\ \quad \mathcal{M}: \quad \varphi'' = \pm\pi/2 \quad \Leftrightarrow \quad X_p = 0 \\ \bullet\ \mathcal{M}_\perp \text{ is in the plane } (z''Ox'') \text{ with } \widehat{z''Ox''} > 0 \text{ towards west} \\ \quad \mathcal{M}_\perp: \quad \varphi'' = 0 \text{ or } \pi \quad \Leftrightarrow \quad Y_p = 0 \end{array} \right.$$

Equations (2) and (15) define the Postel projection completly.

The relation between the transverse cylindrical and the Postel projections is obtained from Eqs. (3) and (1). We have:

$$\left\{ \begin{array}{lclcl} \sin\theta''\cos\varphi'' & = & -\cos\bar{\theta} & = & \sin X \\ \sin\theta''\sin\varphi'' & = & \sin\bar{\theta}\sin\bar{\varphi} & = & \cos X\sin Y \\ \cos\theta'' & = & \sin\bar{\theta}\cos\bar{\varphi} & = & \cos X\cos Y \end{array} \right.$$

and therefore:

$$\left\{ \begin{array}{lcl} X & = & \arcsin(\sin\theta''\cos\varphi'') \\ Y & = & \arctan(\tan\theta''\sin\varphi'') \end{array} \right. \tag{16}$$

The comparison of Eqs. (15) and (16) for the Postel and transverse cylindrical projections respectively shows that for small θ'' (i.e. small areas), the two projection become similar (c.f. lower panels of Figs. 3 and 5). It is also interesting to note that the equations for a gnomic projection in which any straight lines on the map describe a great circle, are:

$$\left\{ \begin{array}{lcl} X_g & = & \tan\theta''\cos\varphi'' \\ Y_g & = & \tan\theta''\sin\varphi'' \end{array} \right. \tag{17}$$

This confirms that Y=constant in Eq. (16) is the equation of a great circle and shows that the lines X=constant are also close to great circles for small θ'' for both the Postel and transverse cylindrical projections. For larger areas, however, the cylindrical projection keep having the lines parallel to one axis describe great circles, which may be a desired feature for local plane-wave analysis, at least along one direction of propagation.

2.3 Tracking

2.3.1 Theory

The main goal of tracking is to remove as much as possible the effect of the solar rotation which would otherwise hide the small horizontal and vertical flows of interest. We consider therefore that the latitude of a point is fixed in time but its Carrington longitude is changing at a rate that is not necessarily the Carrington rate and may depend on the latitude. We use:

$$\left\{ \begin{array}{ll} \psi_{ij}(t_k) = & \psi_{ij}(t_0) \\ \varphi_{ij}(t_k) = & \varphi_{ij}(t_0) + (t_k - t_0)\times \\ & \quad \left[\Omega_0 - \Omega_2\sin^2\psi_0 - \Omega_4\sin^4\psi_0 - \Omega_c\right] \end{array} \right. \tag{18}$$

where Ω_0, Ω_1 and Ω_2 are adjusted to match the sideral differential rotation of the surface and $\mathbf{\Omega}_c \equiv 14.1844$ **deg/day is the sideral Carrington rate** which corresponds to rotation period of $P_c = 25.38$ days). We note that the tracking is done for all points at the rate corresponding to the heliographic latitude of the center of the area. All points lying on a great circle are therefore still on a great circle after tracking. For large areas the differential rotation may vary substantially across the area and therefore one may consider tracking each point using its heliographic latitude (i.e. $\psi_{ij}(t_0)$ instead of ψ_0 in Eq. (18)). However, in the resulting sheared coordinate system, the Y_j =constant lines would no longer describe great circles and it is probably better to still track the full area at a mean rate.

2.3.2 Central Meridian Distance (CMD)

In practice however an alternative form of Eq. (18) is used. If we note $CMD_{ij}(t_k)$ the Central Meridian Distance of the point $M_{ij}(t_k)$ and $L_0(t_k)$ the Carrigton longitude of the disk center at $t = t_k$, we have:

$$CMD_{ij}(t_k) = \varphi_{ij}(t_k) - L_0(t_k) \tag{19}$$

and Eq. (18) becomes:

$$\begin{aligned} CMD_{ij}(t_k) = \quad & CMD_{ij}(t_0) + L_0(t_0) - L_0(t_k) + \\ & (t_k - t_0) \times \left[\Omega_0 - \Omega_2 \sin^2 \psi_0 - \Omega_4 \sin^4 \psi_0 - \Omega_c\right] \end{aligned} \tag{20}$$

If we now assume that the rate at which the the heliographic longitude of the disk center changes is the same at all t_k not too far from t_0,

$$dL_0(t_0) = \frac{L_0(t_k) - L_0(t_0)}{t_k - t_0} = \frac{L_0(t_{1-N_t/2}) - L_0(t_{N_t/2})}{(N_t - 1)\Delta t}, \tag{21}$$

we obtain:

$$\boxed{\begin{aligned} CMD_{ij}(t_k) = \quad & CMD_{ij}(t_0) + (t_k - t_0)\times \\ & \left[\Omega_0 - \Omega_2 \sin^2 \psi_0 - \Omega_4 \sin^4 \psi_0 - d\Omega(t_0)\right] \end{aligned}} \tag{22}$$

where:

$$d\Omega(t_0) = \Omega_c + dL_0(t_0) \tag{23}$$

is the sideral-synodic correction (SSC) at $t = t_0$. Note that with the definition above $dL_0(t_0)$ is negative (i.e. the Carrington longitude of the disk center decrease with time) and therefore we implicitly assume that all t_k are for the same Carrington rotation number (otherwise, with this definition, dL_0 would become positive when L_0 jumps from 0° to 360°).

2.3.3 Sideral-Synodic Correction: 1- Wittmann (1996) formula

The mean SSC for a circular orbit and no inclination of the solar rotation axis would be given by:

$$<d\Omega>= \frac{360}{L_{tyr}} = 0.9856474 \text{ deg/day} = 31.688765 \text{ nHz}$$

where $L_{tyr} = 365.242191$ days is the lenght of the tropical year (equinox to equinox). However, due to the ellipticity ($e \sim 0.0167$) of the Earth's orbit and the inclination of the solar rotation axis with respect to the normal in the plane of the ecliptic, the SSC is changing slightly during the course of the year. Wittmann (1996)[1] gives:

$$d\Omega'(t_0) = <d\Omega> \frac{\cos\Psi(t_0)}{r(t_0)^2} \quad [\text{deg/day}] \tag{24}$$

and:

$$\Psi(t_0) = \arctan\left[-\cos(\lambda_0(t_0) - \omega)\tan i\right] \tag{25}$$

where:

- $\Psi(t_0)$ is the angle between the direction to the pole of the ecliptic and the rotation axis of the Sun,
- $r(t_0)$ is the distance in au between the observer (i.e., the Earth) and the Sun,
- $\lambda_0(t_0)$ is the apparent ecliptic longitude of the Sun,
- $\omega \sim 75.7$ deg is the ecliptic longitude of the ascending node of the solar equator (see Eq. (27) below for a more accurate time-dependent value),
- $i = 7.25$ deg is the inclination of the Sun's rotation axis with respect to the normal in the plane of the ecliptic.

If we note:

- $JD(t_0)$ the Julian day number and fraction,
- $J_{2000}(t_0) = JD(t_0) - 2451545.0$ the number of days and fraction since 2000 January 1 12h00 UT,
- $q(t_0)$ the mean longitude of the Sun corrected for aberration and,
- $g(t_0)$ the mean anomaly,

$\lambda_0(t_0)$ and $r(t_0)$ can be be obtained to a precision of $0°.01$ for t_0 between 1950 and 2050 by (cf. The Astronomical Almanac (2000)):

$$\begin{cases} q(t_0) = & 280.460 + <d\Omega> \; J_{2000}(t_0) \quad [\text{deg}] \\ g(t_0) = & 357.528 + 0.9856003 \; J_{2000}(t_0) \quad [\text{deg}] \\ \lambda_0(t_0) = & q(t_0) + 1.915\sin\left(g(t_0)\right) + 0.020\sin\left(2g(t_0)\right) \; [\text{deg}] \\ r(t_0) = & 1.00014 - 0.01671\cos\left(g(t_0)\right) - 0.00014\cos\left(2g(t_0)\right) \quad [\text{au}] \end{cases} \tag{26}$$

2.3.4 Sideral-Synodic Correction: 2- Ephemeris formula

Another expression for $d\Omega(t_0)$ can be obtained directly from Eqs.(21) and (23) provided that we know $L_0(t)$. These values can be found in the headers of the images themselves (FITS keyword: L0) or can be estimated by the following formulae (see e.g. Eq.(30) of Smart (1960)):

$$\omega(t) = 73°20' + 50''.25 \frac{JD(t) - T_0}{L_{tyr}} \tag{27}$$

[1] In Wittmann (1996) the quantity 0.98<u>65</u> deg/day appears twice (Eq. (2) and above) in place of 0.98<u>56</u> deg/day which I believe is the correct value and is quoted at the end of his article.

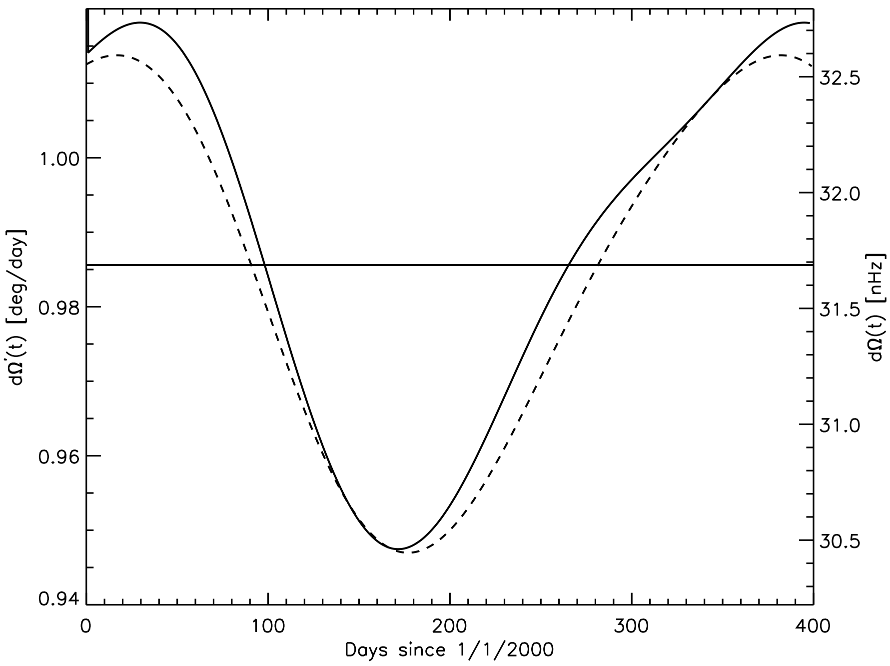

Figure 6: Sideral-Synodic correction as a function of the day since January 1st 2000. **The dashed line** is obtained using Eq. (24) (Wittmann (1996) formula). **The full line** is obtained using Eqs. (28) and (33) (ephemeris formula).

and:

$$L_0(t) = \Big\{ \arctan\left[\tan\big(\lambda_0(t)-\omega(t)\big)\cos i\right]\frac{180}{\pi} + 90\left[\mathrm{sgn}\big(\cos\big(\lambda_0(t)-\omega(t)\big)\big)+1\right] - \Omega_c(JD(t)-T_1)\Big\}\ [360] \tag{28}$$

where:

- $T_0 = 2396757.5$ is the Julian Day number for 1849 Dec. 31st 0h00 UT;
- $T_1 = 2398220.0$ is the Julian Day number for 1854 Jan. 1st 12h00 UT;
- sgn(x)$\equiv x/|x|$;

Note that a similar formula (or more precise ?) has probably been used together with some interpolation to produce the values written as the L0 FITS keyword in each image. Equation (28) is strictly equivalent to the formula used in Frank Hill's FORTRAN subroutine *ephem*.

2.3.5 Conclusion on implementing the varying SSC

Figure 6 shows the difference between the two ways of estimating the time varying SSC. The one currently used is shown by the dashed line (Wittmann (1996) formula). The difference between the two formulae never exceed 0.2 nHz = 0.005

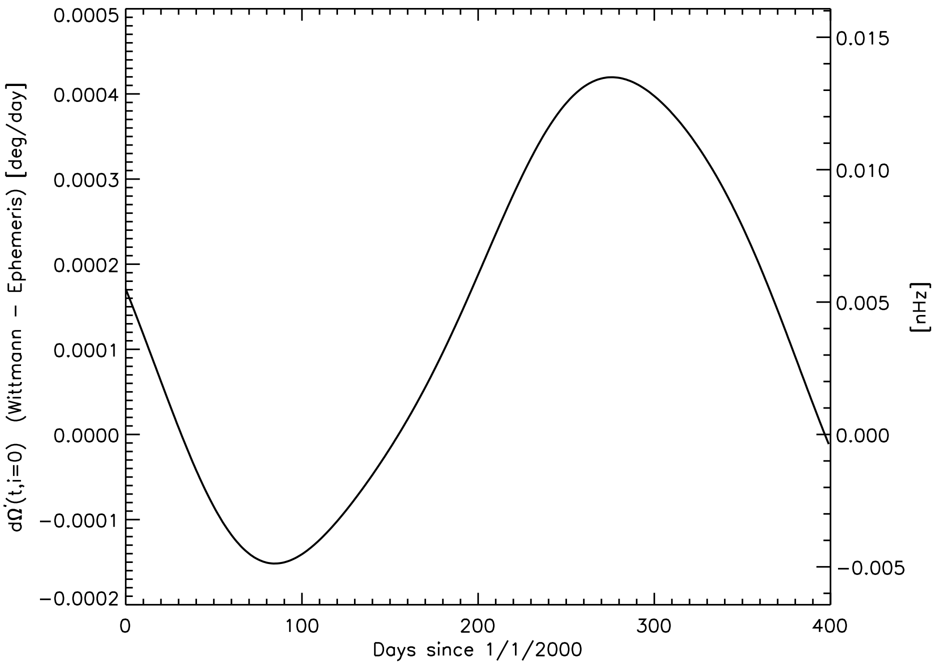

Figure 7: Difference between the two estimates of the SSC due to the ellepticity of the Earth's orbit only ($i = 0$): Eq. (29)-Eq. (31). The two formulae gives essentially the same result.

deg/day which is bellow the internal precision expected for each formula. The fact that ω, the ecliptic longitude of the ascending node of the solar equator, was taken constant in Wittman formula does not contribute to the difference (From Eq. (27) ω increase only by $50.25/3600 = 0.014°$ during the year). In order to check the effect of the Earth elliptic orbit only, we can artificially take $i = 0$ (no inclination of the solar rotation axis). In that case Wittmann (1996) formula gives:

$$
\begin{aligned}
d\Omega(t_0, i=0) &= \frac{<d\Omega>}{r(t_0)^2} && (29)\\
&= \frac{<d\Omega>}{\left[1.00014 - 0.01671\cos\left(g(t_0)\right) - 0.00014\cos\left(2g(t_0)\right)\right]^2} && (30)
\end{aligned}
$$

while from Eq. (28) we obtain for $t_k - t_0 = 1$ day (and assuming that t_k and t_0 correspond to the same Carrington rotation number)

$$
\begin{aligned}
d\Omega(t_0, i=0) &= \lambda_0(t_0) - \lambda_0(t_k) + \omega(t_k) - \omega(t_0)\\
&= <d\Omega> +1.915\left\{\sin\left(g(t_0)\right) - \sin\left(g(t_0) + 0.9856003\right)\right\} && (31)\\
&\quad +0.020\left\{\sin\left(2g(t_0)\right) - \sin\left(2(g(t_0) + 0.9856003)\right)\right\}
\end{aligned}
$$

Note that $\omega(t_k) - \omega(t_0) = 50.25/(3600\ L_{tyr}) \simeq 410^{-5}$ has been neglected. The difference between these two formulae is plotted as a function of the day of the year 2000 on Fig. 7. It remains extremely small (< 0.0005 deg/day) which in turn indicates that the difference (c.f. Fig. 6) between the two approaches must reside essentially in the different ways of estimating the effect of the inclination of the Sun's rotation axis.

The explicit value of the SSC is however not needed (!) as it is already implicitly contained in the values of $L0$ present in the header of each image. **Therefore, it would be more consistent and potentially more accurate (if the ephemeris table from which the header values are derived are more accurate than the low precision formula presented here) to read these values from the images headers and use only Eq. (18) for the tracked longitudes and Eq. (19) for the corresponding CMDs which are the only two quantities really needed! This would also allow us to use directly MDI (or other) data provided that the L0 values contained in the image headers take into account the motion of the observer (or spacecraft) with respect to the Sun.**

There is however one practical reason why this has not been done until now: the Central Meridian Distance are easier to manipulate than the Carrington longitudes because we may have a jump in the Carrington longitudes (from 359° to 0°) that define an area on a solar image while this doesn't happen with the CMDs. By definition the CMD is taken such that $-\pi \leq CMD < \pi$, therefore 2π may have to be added or substracted to Eq. (19) when we compute the CMD from the Carrington longitude and L_0. By definition φ and L_0 are between 0 and 2π and therefore the CMD as defined in Eq. (19) is between -2π and 2π. The following can be applyed to convert the CMD in the correct range:

$$\left\{ \begin{array}{l} CMD'_{ij}(t_k) = CMD_{ij}(t_k) + \alpha_{ij}(t_k) \\ \alpha_{ij}(t_k) = -180\ sign\big(CMD_{ij}(t_k)\big)\ \big(sign\big(|CMD_{ij}(t_k)| - 180\big) + 1\big) \end{array} \right. \tag{32}$$

Similarly, $dL_0(t_0)$ should rigourously be defined by taking into account the jumps in L_0 at the transition between two Carrington rotation numbers.

$$\left\{ \begin{array}{ll} dL'_0(t_0) = & dL_0(t_0) + \beta(t_0, t_k)/(t_k - t_0) \\ \beta(t_0, t_k) = & -360(C_r(t_k) - C_r(t_0)) \\ d\Omega'(t_0) = & \Omega_c + dL'_0(t_0) \end{array} \right. \tag{33}$$

where $C_r(t)$ is the Carrington rotation number at the time t. With these notation we obtain:

$$\boxed{\begin{array}{ll} CMD'_{ij}(t_k) = & CMD'_{ij}(t_0) + \alpha_{ij}(t_k) - \alpha_{ij}(t_0) + \beta(t_k, t_0) + \\ & (t_k - t_0)\left[\Omega_0 - \Omega_2 \sin^2 \psi_0 - \Omega_4 \sin^4 \psi_0 - d\Omega'(t_0)\right] \end{array}} \tag{34}$$

These equations are the more rigourous and correct forms of Eqs. (19)-(23). However, all we do here is to add multiples of 360° and therefore, if we need only the values of trigonometric functions of the CMDs, we can directly use the quantities defined by Eq. (19) or Eq. (22) to compute these values.

2.4 Orthographice projection on the Camera plane [To be completed]

Once we know the heliographic coordinates of the points of interest we need to look for them on our solar images $I(t_k)$. The solar disc is shown on GONG+ merged

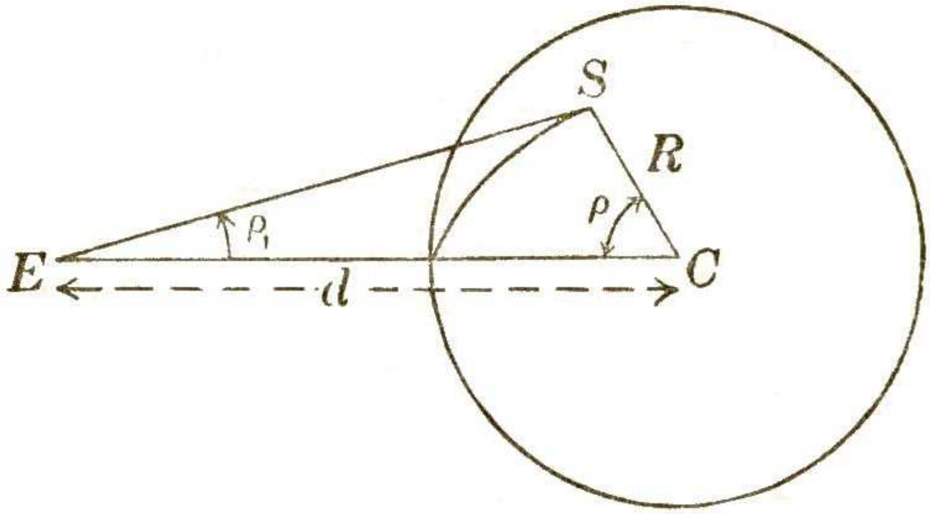

Figure 8: From Smart (1960) **[To be completed]**

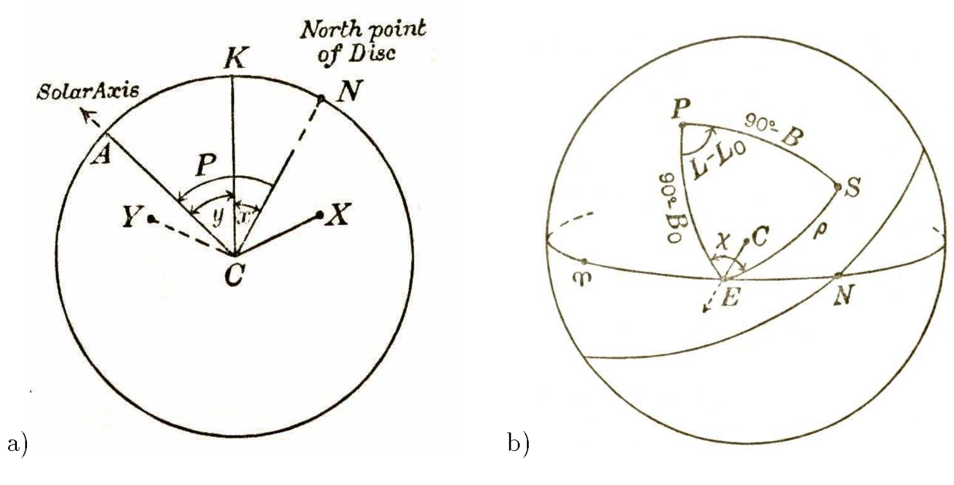

Figure 9: From Smart (1960) **[To be completed]**

images as a circle of radius r_o pixels. They are registered so that the Solar north is on top of the y axis and the east on the left. The coordinates (η, ξ) from the lower left corner of the image taken at t_k of the points $M_{ij}(t_k)$ are then obtained by doing a projection at Earth distance. If we note $\psi \equiv \psi_{ij}(t_k)$ and $\varphi \equiv \varphi_{ij}(t_k)$, we obtain:

$$M_{ij}(t_k) = I_{\eta\xi}(t_k) \tag{35}$$

where:

$$\left\{ \begin{array}{rl} \frac{\eta-\eta_c}{r_o} = & \cos\psi \sin(\varphi - L_0)/(1 - S\alpha) \\ \frac{\xi-\xi_c}{r_o} = & \frac{\sin\psi\cos B_0 - \cos\psi \sin B_0 \cos(\varphi - L_0)}{1-S\alpha} \end{array} \right. \tag{36}$$

$$\alpha = \sin\psi \sin B_0 + \cos\psi \cos B_0 \cos(\varphi - L_0)$$

The position of the disc center (η_c, ξ_c), its heliographic coordinates (L_0, B_0), the Sun apparent semi-diameter in radian S and r_0 can be found in the FITS header of each image[2].

[To be completed for site/non registered images]

2.5 Interpolation

The values of (η, ξ) computed from Eq. (36) are in general not integers and therefore we need to interpolate between the images' pixels. We have implemented 3 different interpolators.

2.5.1 The 'ideal' sinc interpolator'

The 'ideal' sinc interpolator is defined in 1D by:

$$I_x = \sum_{n=-N_s}^{N_s-1} \frac{\sin(\pi(x-n))}{2N_s \tan\left(\frac{\pi(x-n)}{2N_s}\right)} I_n \tag{37}$$

where N_s defines the length of the interpolator. The 2D interpolation is obtained by applying Eq. (37) successively in each direction. This can be seen as a tapered version of the sinc interpolator where the taper is 'ideal' for the Discrete Fourier Transform (DFT) in the sense that if we were to shift the image by an arbitrary fraction of a pixel using this interpolator, with N_s equal to the number of pixels in both directions, the DFT would remain the same except for a phase difference. A similar interpolator (with a slightly different tapering function) is used during the merging of individual site images and it is probably a good idea to keep the same interpolator in both steps.

2.5.2 The 'Lookup' sinc interpolator

In our current implementation, the computations needed for the sinc interpolation are time consuming. This difficulty can be overcomed by using a lookup table for the trigonometric quantities resulting in the so-called lookup sinc interpolator which has also been implemented for arbitrary precision p in the lookup tables. An equivalent and probably more efficient approch would be to do an ideal time domain interpolation by (1) taking the FFT, (2) zero-padding in the frequency domain and

[2]Respectively by the keywords: FNDLMBXC, FNDLMBYC, L0, B0, SEMIDIAM and C_MA

(3) taking the inverse FFT. The amount of zero-padding is in that case related to the precission p used for our lookup tables.

2.5.3 The spline interpolator [To be completed]

Since we are interpolating the image at arbitrarily distributed points, we are not only shifting but also stretching the image. Moreover, the sinc interpolator is never used on the full extent of the image but rather locally around each point with N_s small. Therefore it is not completely obvious that the tapered sinc interpolator is ideal in our case and we have also implemented a spline interpolator based on a tensorial product of B-splines (De Boor, 1978) of arbitrary order m_s. It presents a good frequency response even for low order splines and its computation is based on finite differences which are very easy and fast to implement.

Generally speaking a 2D interpolation at an arbitrary point (x, y) by a tensorial product of B-spline can be written as:

$$I(x,y) = \sum_{p=1}^{N_x} \sum_{q=1}^{N_y} c_{pq} \; \varphi_p(x) \; \psi_q(y) \tag{38}$$

where $\{\varphi_p(x)\}_{p=1..N_x}$ and $\{\psi_q(y)\}_{q=1..N_y}$ are B-spline basis of order m_x and m_y (i.e. peicewise polynomial of degree $m_x - 1$ and $m_y - 1$). In our case we consider an isotropic basis with $N_x = N_y = N_s$, $m_x = m_y = m_s$ and $\varphi_p(x) \equiv \psi_p(x)\ \forall p$. Only m_s splines are non zero at any given x: from $p = l(x) - 1 + m_s$ to $p = l(x)$ where $l(x)$ is a function of x that depends on the properties of the spline basis chosen. Therefore we can write:

$$I(x,y) = \sum_{p=l(x)-m_s+1}^{l(x)} \quad \sum_{q=l(y)-m_s+1}^{l(y)} c_{pq} \; \varphi_p(x) \; \varphi_q(y) \tag{39}$$

The coefficients c_{pq} are found by writting Eq. (39) at the points $(i,j)_{\substack{i=1..N_s \\ j=1..N_s}}$ where the image value is known:

$$I_{ij} = \sum_p \sum_q c_{pq} \; \varphi_{pi} \; \varphi_{qj} \tag{40}$$

or, in matricial form:

$$I = \varphi^{\top} \; C \; \varphi \tag{41}$$

from which we get the coefficients C_{pq} by:

$$C = (\varphi^{\top})^{-1} \; I \; \varphi^{-1} \tag{42}$$

The computation are based on the concept of 'nodal vector' that defines uniquely and completly a B-spline basis. The 2 routines used are:

- **spl_interpol_init:** Sets the grid coordinates to $1..Ns$, build the nodal vector and Compute C
- **spl_interpol:** Computes $I(x, y)$ for any $1 \leq x \leq N_s$ and $1 \leq y \leq N_s$ using Eq. (39) and knowing C and the nodal vector.

For this, they use:

- **spl_snoeink:** Builds the nodal vector $y(1 : N_s + m_s)$ of the B-spline basis from the grid coordinates at which the image is known, the order m_s and the multiplicity k_s. The interpolating function will be a peicewise polynomial of degree $m_s - 1$ with $m_s - k_s - 1$ derivative continue at the nodal points. $k_s = 1$ is usually taken. If not, we must insure $mod(N_s - m_s, k) = 0$. Adapted from De Boor (1978) p. 219 Eq. (10).

- **spl_slinfkv:** Gives l(x) knowing the nodal vector y. This is a simplified version assuming that the grid coordinates are just integers from 1 to N_s. The nodal vector is actually not used, it is assumed that is is built using spl_snoeink with m_s and k_S. Notice that we always have $y(l(x)) \leq x < y(l(x)+1)$.

- **spl_bvalv:** Computes the m_s splines that are non zero at a point x knowing the nodal vector y and $l(x)$ i.e. it gives φ_p for $p = l(x) - m_s + 1$ to $p = l(x)$. Adapted from Schumaker (1981) algorithm 5-5 p. 192.

- **spl_sbsp2dkv:** Computes C from I using Eq. (42) and knowing the nodal vector and the grid coordinates.

2.5.4 Conclusion on the choice of the interpolator

By plotting the difference of the power spectra obtained from spline and sinc interpolator we realized that differences exist which are principally concentrated on the rings. These differences are however very small and the relative difference is essentially zero for absolute values of the horizontal wave number below 1 rad/Mm^{-1}. Therefore it seems that only the very outer rings could potentially be affected by the choice of the interpolation.

2.6 The 'dense pack' of data cubes

In order to study an extended area of the solar surface we process a collection of 189 data cubes centered at different heliographic latitudes and longitudes (ψ_0, φ_0) on the reference image $I(t_0)$.

$$\begin{cases} \psi_0(u,v) = \quad u \times 7.5°, & u = -7..7 \\ \varphi_0(u,v) = L_0(t_0) + v \times 7.5°, & v = -h_{|u|}..h_{|u|} \end{cases} \tag{43}$$

where $h = [7, 7, 7, 7, 6, 6, 4, 3]$.

For the present work, we have done three dense-pack analyses for t_0 corresponding to January 2002 11-13 with corresponding $L_0(t_0) = 300°, 285°, 270°$ respectively. We used the same parameters as in previous analyses of MDI data (e.g. Haber et al.,2002): the grid is defined by $N_x = N_y = 128$, $\Delta x = \Delta y = 0.125°$, $N_t = 1664$, $\Delta t =$ 1mn=1/1440 day; the tracking rate is given by $\Omega_0 = 451.43$nHz, $\Omega_2 = 54.77$nHz, $\Omega_4 = 80.17$nHz and the interpolator chosen is based on cubic splines ($m_s = 4$).

3 Multitaper analysis, ring fitting and inversion [To be completed]

Each data cube is then Fourier transformed via a 3D FFT. This requires first a spatial and a temporal apodization in order to avoid truncation effects. We have chosen a 2D cosine bell apodization in the spatial direction reducing a $16° \times 16°$ area to a circular patch of radius 15°.

The temporal apodization is carried out using a multitaper technique which first multiplies a sequence of orthogonal sine tapers to the window function, re-orthogonalizes them, applies a temporal FFT to each tapered time series and then averages the resultant power spectra. Doing so, we avoid the lost of data that would result from the use of a single taper and obtain a better distribution of the power along the rings. Applying too many tapers would result in an over-smoothed power spectrum and therefore a trade-off has to be found. In this work, we used 3 sine multitapers (Fodor & Stark, 1998).

The last steps of the analysis consist in fitting the rings in the power spectra (see Fig. 10) and inverting the inferred frequency shifts to obtain the depth dependence of the flow. This has been done using the code developed for MDI and described in Bogart et al. (1995).

4 First results: Comparison with MDI [To be completed (work with D. Haber)]

A study of the errors as a function of depth have shown that the lowest errors are reached at a depth of about 1-2Mm. We have therefore chosen this depth for the first comparison between GONG and MDI ring diagram analysis. The differences between the flows obtained from the two datasets at a depth of 1.18 Mm are shown in Fig. 11. The amplitudes of the differences are clearly a function of the distance from the center of the disk. They remain small at the very center but can reach very high relative amplitudes at the edges. For the second day, a clear systematic difference in the orientation of the flow is found. This reflects the fact that the GONG flow for that day has been found with a significant curl. A problem with the P-angle could produce such apparent rotating flow but we couldn't identify clearly the source of the problem and why this happened only for that particular day which had a very good duty cycle of 91.2%. Clearly this is very preliminary work using the new GONG+ data product and more investigations and quantitative analysis are needed to better understand the systematic errors that may be present in both GONG and MDI data analysis.

Acknowledgments

This work utilizes data obtained by the Global Oscillation Network Group (GONG) project, managed by the National Solar Observatory, which is operated by AURA, Inc. under a cooperative agreement with the National Science Foundation.

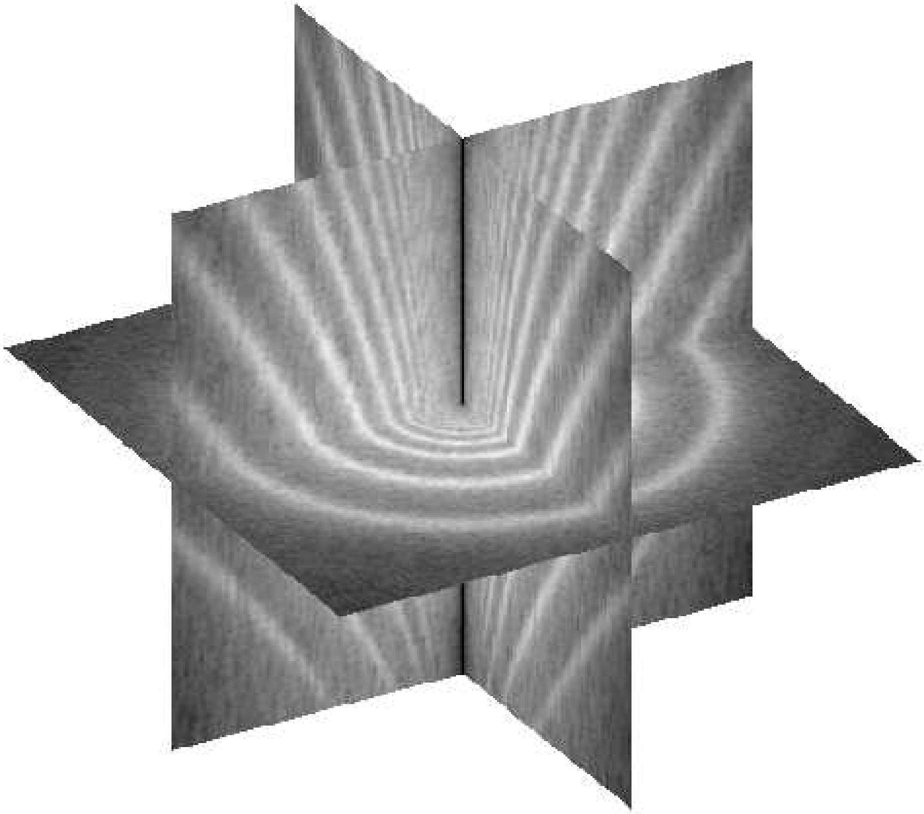

Figure 10: An example of 3D power spectra showing the characteristic rings of power distorted by the underlying flows. The two horizontal axis are k_x k_y while the vertical axis give the frequencies.

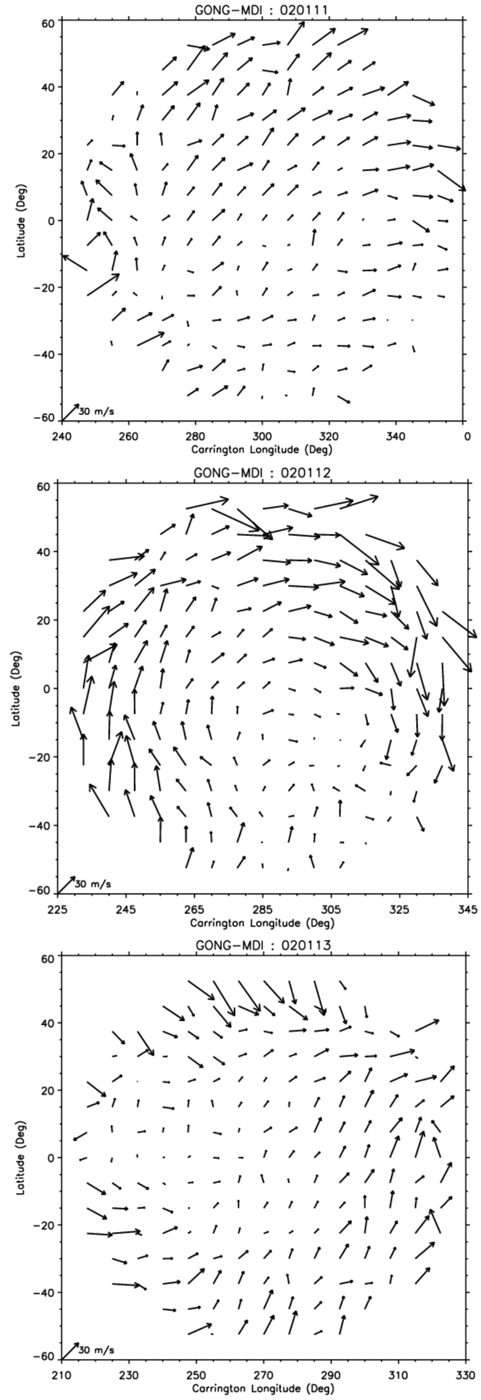

Figure 11: Difference between the flows at a depth of 1.18Mm inferred from GONG and MDI data for 3 consecutive days (January 11-13 2002 from top to bottom).

References

Astronomical Almanac 2000, Published by the Nautical Almanac Office, United States Naval Observatory in cooperation with Her Majesty's Nautical Almanac Office, p. C24 [see also http://aa.usno.navy.mil/faq/docs/SunApprox.html]

Bogart R. S., Sá L. A. D., Duvall T. L., Haber, D. A., Toomre J., and Hill F., 1995, in J. T. Hoeksema, V. Domingo, B. Fleck, and B. Battrick (eds), Proc. Fourth SOHO Workshop: Helioseismology, ESA SP-376, Vol. 2, p. 147

De Boor C., 1978, A Practical Guide to Splines, Springer Verlag.

Fodor & Stark, 1998, in S. Korzennik and A. wilson (eds), Structure and Dynamics of the Interior of the Sun and Sun-like Stars, ESA SP-418, p. 171

Haber D., Toomre, J., Hill F., Gough D., 1995, in R. K. Ulrich, E. J. Rhodes, Jr, and W. Däppen (eds), GONG'94: Helio- and Astero-seismology from the Earth and Space, ASP Conf Series 76, p. 272

Haber A. D., Hindman B. W., Toomre J., Bogart R. S., Larsen R. M., Hill F., 2002, ApJ 570, 855

Hill F., Bolding J., Toner C., et al., 2003, this proceeding.

Postel G., Polo Aptata Nova Charta Universi, 1581, Bibliothèque Nationale, Paris

Schumaker, Lary L., 1981, Spline Functions: Basic Theory, John Wiley and Sons, New York Chichester Brisbane Toronto.

Smart W. M., 1960, Text-Book on Spherical Astronomy, 6th ed. Cambridge, England: Cambridge University Press.

Toner C., Haber D., Corbard T., Bogart R., 2003, An Image Merge For GONG+, SOHO12/GONG 2002 proceeding.

Wittman A. D., 1996, Sol. Phys. 168, 211